Resolvent-based estimation of wavepackets in turbulent jets

Aaron Towne*, Rutvij Bhagwat[†], Yuhao Zhou[‡], Junoh Jung[§]
University of Michigan, Ann Arbor, MI 48109, USA

Eduardo Martini[¶], Peter Jordan[‖]
Institut PPrime, CNRS–Université de Poitiers–ENSMA, 86000 Poitiers, France

Diego B. S. Audiffred**, Igor Maia[††], André V. G. Cavalieri[‡‡]
Instituto Tecnológico de Aeronáutica, São José dos Campos, SP, Brazil

We aim to reduce the noise emitted by high-speed turbulent jets using recently developed resolvent-based estimation and control tools. Our approach relies on detecting noise-generating wavepackets and canceling them via actuation. This paper reports on our progress toward this objective in the form of (i) implementation and validation of these resolvent-based tools in a large-scale CFD solver and (ii) preliminary estimation results for a subsonic jet. We validate our implementation via comparisons to the literature for a laminar channel flow, the acoustic response to a monopole forcing in a freestream, a trailing-line vortex problem, an airfoil wake, and resolvent modes for a jet. The preliminary estimation study for the subsonic jet shows that operator-based and data-driven versions of the methods yield similar estimation kernels and results. Future work will focus on extending this study to a series of supersonic jets and systematically exploring the selection and placement of sensors, actuators, and targets to mitigate noise-generating wavepackets most effectively.

I. Introduction

Efforts to reduce jet noise have been underway for decades but have led to modest improvements. Historically, passive noise control strategies, such as chevrons and nozzle inserts, and open-loop flow control approaches have been extensively used but have had only modest success (on the order of a few dB) in achieving jet noise reduction [1]. As a result, more recently, closed-loop control has emerged as a potential candidate for achieving a more significant noise reduction by identifying and canceling noise-generating wavepackets [2, 3]. Resolvent-based estimation and control is a promising candidate for this purpose because resolvent analysis has been shown to efficiently model large-scale

---

*Assistant Professor, Department of Mechanical Engineering & AIAA Senior Member
[†]Research Fellow, Department of Mechanical Engineering
[‡]Graduate Student Research Assistant, Department of Mechanical Engineering
[§]Graduate Student Research Assistant, Department of Mechanical Engineering
[¶]Professor, Département Fluides Thermique et Combustion
[‖]Professor, Département Fluides Thermique et Combustion
**Graduate Student, Division of Aeronautical Engineering
[††]Post-Doctoral Research Fellow, Département Aérodynamique, Énergétique et Propulsion
[‡‡]Professor, Division of Aeronautical Engineering

wavepacket structures [4] and the near and far-field noise they emit [5, 6].

This work follows a series of studies investigating the use of resolvent analysis for estimation and control. Resolvent analysis can be a powerful tool for a low-rank reconstruction of flow statistics if the nonlinear forcing statistics are known or can be reasonably modeled [7]. A common choice of the model is to assume no preferential forcing direction, in which case the reconstruction solely relies on the properties of the resolvent operator [8, 9]. Towne et al. [10] used sparse measurements/data to determine the statistics of the nonlinear forcing, which are then used to reconstruct flow statistics after the action of the resolvent. Martini et al. [11] extended this work to obtain optimal non-causal estimates of time-varying flow quantities. Amaral et al. [12] used this framework to estimate velocity fluctuations in a turbulent channel flow from low-rank shear stress and/or pressure measurements at the wall. To adapt these non-causal methods for real-time estimation and control, Martini et al. [13] used a Wiener-Hopf formalism to enforce causality. Jung et al. [14] and Jung and Towne [15] used these tools to estimate fluctuations in the laminar and turbulent wakes of an airfoil.

Our current work aims to use these resolvent-based estimation and control tools to mitigate the noise emitted by high-speed turbulent jets. This follows on recent work in which these tools have been used to control wavepackets in experiments [3, 16]. The results show great promise, but the ability to systematically explore sensor and actuator configurations and work at high Mach numbers has been limited by practical experimental restrictions. The present paper represents a first step toward applying these resolvent-based tools within simulations of high-speed jets, which will enable systematic exploration of sensor and actuator placements and types and application to high Mach numbers. The long-term objective of this work is to build a realistic strategy for turbulent jet noise control, a highly relevant technological challenge for commercial or military aircraft.

The remainder of this paper is organized as follows. The numerical framework is discussed in Sec. II, and some validation tests for our code are presented in Sec. III. Preliminary results for a subsonic jet configuration are discussed in Sec. IV, and the paper is concluded, along with a discussion of future work, in Sec. V.

II. Numerical Framework

A. Numerical Method

In this work, we solve the three-dimensional compressible Navier-Stokes equations for a perfect gas,

$$\frac{\partial}{\partial t}\begin{pmatrix} \rho \\ \rho u_i \\ \rho E \end{pmatrix} + \frac{\partial}{\partial x_j}\begin{pmatrix} \rho u_j \\ \rho u_i u_j + p\delta_{ij} \\ (\rho E + p)u_j \end{pmatrix} = \frac{\partial}{\partial x_j}\begin{pmatrix} 0 \\ \tau_{ij} \\ \tau_{kj}u_j - q_j \end{pmatrix}. \tag{1}$$

Here, ρE is the total energy, and the ideal gas law, $p = \rho RT$, closes the equations. The heat flux q_j is given by Fourier's Law, $q_j = -\kappa \frac{\partial T}{\partial x_j}$, and the Newtonian viscous stress tensor is

$$\tau_{ij} = \mu \left(\frac{\partial u_i}{\partial x_j} + \frac{\partial u_j}{\partial x_i} - \frac{2}{3} \frac{\partial u_k}{\partial x_k} \delta_{ij} \right).$$

We use the unstructured LES solver CharLES for this work. The reader is referred to Brès et al. [17] for the details of the solver and the numerical schemes used.

B. Linearization

We use the framework of CharLES to implement the linearization and to build the tools for estimation and control. The Navier-Stokes equations can be described in the operator form

$$\frac{\partial q}{\partial t} = \mathcal{F}(q), \tag{2}$$

where q is the global state vector containing all the degrees of freedom in the system and $\mathcal{F}$ is the nonlinear Navier-Stokes operator. The state vector can be decomposed into a mean component $\bar{q}$ and a perturbation q',

$$q(x, t) = \bar{q}(x) + q'(x, t). \tag{3}$$

Introducing this decomposition in Eq. (2), we get

$$\frac{\partial q'}{\partial t} = Aq' + f'. \tag{4}$$

Here, $A = \frac{\partial \mathcal{F}}{\partial q}(\bar{q})$ is the linearized Navier Stokes operator, and f' can be considered as the collection of nonlinear terms or an external forcing on the system.

In this work, we explicitly form the linearized Navier-Stokes operator A, typically known as the matrix-forming approach. The linearization is performed using the framework of the LES solver CharLES. Extracting linear operators from a large-scale CFD solver can be a complex task. Naively, this can be done by perturbing each degree of freedom individually,

$$A(:, j) = \frac{\mathcal{F}(\bar{q} + \epsilon e_j) - \mathcal{F}(\bar{q})}{\epsilon}, \tag{5}$$

where $e_j \in \mathbb{R}^N$ is the j-th unit vector and N is the dimension of the discretized sate, i.e., $q \in \mathbb{R}^N$. However, this approach is extremely expensive, as the number of times the operator $\mathcal{F}$ must be evaluated scales with the size of the problem N. Instead, we adopt an approach that relies on perturbing multiple degrees of freedom simultaneously. Specifically, we simultaneously perturb degrees of freedom with non-overlapping numerical stencils, allowing many columns of A to be simultaneously computed, similar to the approach adopted by Nielsen and Kleb [18] and more recently by Cook et al. [19]. In this approach, the number of function evaluations does not scale with the size of the

problem and instead only depends on the numerical schemes used. In our case, the sorting of the domain into lists of non-overlapping degrees of freedom is carried out on a single processor, and that information is then broadcast to all other processors. The open-source package PETSc [20, 21] is used for storing the operators and efficiently performing subsequent large-scale linear algebra computations associated with the linear operator.

Stability analysis often involves problems where the mean flow $\bar{\boldsymbol{q}}$ is invariant in one or more directions, in which case the perturbation $\boldsymbol{q}'$ can be decomposed into decoupled Fourier modes in these homogeneous directions. In round jets, the mean flow is typically axisymmetric, such that the perturbation can be decomposed into Fourier modes with different azimuthal wavenumbers m, i.e.,

$$\boldsymbol{q}(x, r, \theta, t) = \bar{\boldsymbol{q}}(x, r) + \boldsymbol{q}'(x, r, \theta, t) \tag{6}$$

with

$$\boldsymbol{q}'(x, r, \theta, t) = \hat{\boldsymbol{q}}(x, r) e^{i(m\theta - \omega t)}. \tag{7}$$

Our code seamlessly handles these scenarios following a procedure outlined in Bhagwat [22]. Roughly stated, the idea is to perform two-dimensional simulations in the $x - r$ plane and account for azimuthal terms via the addition of specific source terms. This allows individual azimuthal modes to be independently investigated at a low computational cost.

C. Estimation Framework

We consider a linear dynamical system similar to one in Eq. (4) driven by both forcing $\boldsymbol{f}(t)$ and actuation $\boldsymbol{a}(t)$. Linearity allows us to decouple the system into its forcing and actuation-driven components. The forcing-driven part is given as

$$\frac{d\boldsymbol{q}_1}{dt}(t) = \boldsymbol{A}\boldsymbol{q}_1(t) + \boldsymbol{B}_f \boldsymbol{f}(t), \tag{8}$$

$$\boldsymbol{y}_1(t) = \boldsymbol{C}_y \boldsymbol{q}_1(t) + n(t), \tag{9}$$

$$z_1(t) = \boldsymbol{C}_z \boldsymbol{q}_1(t) \tag{10}$$

and the actuation-driven part is given as

$$\frac{d\boldsymbol{q}_2}{dt}(t) = \boldsymbol{A}\boldsymbol{q}_2(t) + \boldsymbol{B}_a \boldsymbol{a}(t), \tag{11}$$

$$\boldsymbol{y}_2(t) = \boldsymbol{C}_y \boldsymbol{q}_2(t), \tag{12}$$

$$z_2(t) = \boldsymbol{C}_z \boldsymbol{q}_2(t). \tag{13}$$

Here, $\boldsymbol{f}(t)$, $\boldsymbol{a}(t)$, and $\boldsymbol{n}(t)$ are the forcing, actuation signal, and noise, respectively. $\boldsymbol{B}_a$ and $\boldsymbol{B}_f$ are operators that map the forcing and actuation to the system. The operators $\boldsymbol{C}_y$ and $\boldsymbol{C}_z$ extract the measurement $\boldsymbol{y}(t)$ and the target $\boldsymbol{z}(t)$ from the state vector $\boldsymbol{q}(t)$.

We seek to estimate the target based on sensor readings via the convolution

$$\tilde{\boldsymbol{z}}(t) = \int_{-\infty}^{\infty} \boldsymbol{T}_z(\tau)\boldsymbol{y}(t-\tau)d\tau, \tag{14}$$

which can equivalently be expressed in the frequency domain as

$$\hat{\tilde{\boldsymbol{z}}} = \hat{\boldsymbol{T}}_z \hat{\boldsymbol{y}}. \tag{15}$$

A number of different estimation kernels $\hat{\boldsymbol{T}}_z$ can be derived. An optimal non-causal estimation kernel $\hat{\boldsymbol{T}}_{z,nc}$ can be obtained by minimizing the cost function

$$J_{nc} = \int_{-\infty}^{\infty} E\{\boldsymbol{e}^*(t)\boldsymbol{e}(t)\}\, dt = \frac{1}{2\pi} \int_{-\infty}^{\infty} E\{\hat{\boldsymbol{e}}^*(\omega)\hat{\boldsymbol{e}}(\omega)\}\, d\omega, \tag{16}$$

where $\boldsymbol{e} = \tilde{\boldsymbol{z}} - \boldsymbol{z}$ is the error between the estimated and true state [11]. Minimizing the cost function yields the non-causal estimation kernel

$$\hat{\boldsymbol{T}}_{z,nc} = \hat{\boldsymbol{G}}_r \hat{\boldsymbol{G}}_l^{-1}, \tag{17}$$

where

$$\hat{\boldsymbol{G}}_r = \boldsymbol{R}_{zf}\hat{\boldsymbol{F}}\boldsymbol{R}_{yf}^{\dagger}, \tag{18a}$$

$$\hat{\boldsymbol{G}}_l = \boldsymbol{R}_{yf}\hat{\boldsymbol{F}}\boldsymbol{R}_{yf}^{\dagger} + \hat{\boldsymbol{N}}, \tag{18b}$$

$\hat{\boldsymbol{F}}$ and $\hat{\boldsymbol{N}}$ are the cross-spectral densities (CSDs) of the forcing and noise, respectively, and $\boldsymbol{R}_{yf} = \boldsymbol{C}_y\boldsymbol{R}\boldsymbol{B}_f$, $\boldsymbol{R}_{zf} = \boldsymbol{C}_z\boldsymbol{R}\boldsymbol{B}_f$, $\boldsymbol{R}_{ya} = \boldsymbol{C}_y\boldsymbol{R}\boldsymbol{B}_a$ and $\boldsymbol{R}_{za} = \boldsymbol{C}_z\boldsymbol{R}\boldsymbol{B}_a$ are various specialized forms of the resolvent operator

$$\boldsymbol{R} = (-i\omega\boldsymbol{I} - \boldsymbol{A})^{-1}. \tag{19}$$

Similarly, the optimal causal estimation kernel is obtained by minimizing the cost function in Eq. (16) with additional Lagrange multipliers $\boldsymbol{\Lambda}_-$ to enforce causality [13]. Minimizing this new cost function leads to the condition

$$\hat{\boldsymbol{T}}_{z,c}\hat{\boldsymbol{G}}_l + \hat{\boldsymbol{\Lambda}}_- = \hat{\boldsymbol{G}}_r, \tag{20}$$

5

under the constraint that $\mathbf{\Lambda}_-(t > 0) = 0$ and $\mathbf{T}_{z,c}(t < 0) = 0$. This is a matrix Wiener-Hopf problem that must be solved to obtain the optimal causal kernel $\hat{\mathbf{T}}_{z,c}$. In general, the optimal causal kernel is different from a truncated noncausal kernel $\hat{\mathbf{T}}_{z,tnc}$ obtained by setting the non-causal part of the optimal non-causal kernel $\hat{\mathbf{T}}_{z,nc}$ to zero.

In both cases, the modified resolvent operators $\mathbf{R}_{yf}$, $\mathbf{R}_{zf}$, $\mathbf{R}_{ya}$ and $\mathbf{R}_{za}$ form the building blocks of the estimation (and also the control) kernels. These operators map the forcing and actuation to the sensor measurements and targets. While these operators could, in principle, be formed directly from their definitions, in most cases, it is more computationally efficient to form them in the time domain by integrating the direct ($\mathbf{A}$) or the adjoint ($\mathbf{A}^\dagger$) systems. For instance, $\mathbf{R}_{yf}$ can be assembled through the adjoint system

$$-\frac{d\mathbf{q}_{i,1}}{dt} = \mathbf{A}^\dagger \mathbf{q}_{i,1} + \mathbf{C}^\dagger_{y,i}\delta(t), \qquad \mathbf{p}_{i,1} = \mathbf{B}^\dagger_f \mathbf{q}_{i,1} \,. \tag{21}$$

Each time-domain solution $\mathbf{p}_{i,1}$ yields the i-th column of $\mathbf{R}^\dagger_{yf}$, and the procedure needs to be repeated for each sensor $\mathbf{C}_{y,i}$ to get the full operator. Similarly, other operators can be assembled using different combinations of the various $\mathbf{B}$ $\mathbf{C}$ operators. Moreover, these could also be obtained through the direct system. For high-rank forcings and/or targets, multi-stage runs involving both the direct and the adjoint systems may be required to assemble the operators efficiently. We follow Martini et al. [13] in forming the necessary linear operators via a time-stepping algorithm and using these operators for estimation and control; the reader is referred to that paper for a more detailed discussion. For the interested reader, a discussion of how similar time-stepping methods can be used to efficiently compute resolvent mode, i.e., its leading singular values and vectors, can be found in Martini et al. [23] and Farghadan et al. [24].

A key element of our implementation that differs from that of Martini et al. [13] is our use of checkpointing to minimize memory consumption. Forming the products of resolvent operators that appear in Eq. (18) involves integrating the direct and adjoint linear equations in succession, i.e., the time-varying solution of one run serves as the forcing term for the next run. For large problems, storing these time-varying solutions in memory becomes problematic and reading and writing to disk is slow. To minimize this memory overhead, our implementation includes an optimized check-pointing algorithm, differing from the interpolation technique used by Martini et al. [13], which eliminates the need to store time-series data, with a penalty of roughly 50% higher CPU cost.

D. Data-driven implementation

Martini et al. [13] showed that the estimation and control kernels can be formed using unsteady data from experiments or simulations. Specifically, it can be shown that the matrix coefficients $\hat{\mathbf{G}}_r$ and $\hat{\mathbf{G}}_l$ from which the estimation kernels are formed can be related to the CSDs of the uncontrolled problem, $\hat{\mathbf{G}}_r = \mathbf{S}_{z_1,y_1}$ and $\hat{\mathbf{G}}_l = \mathbf{S}_{y_1,y_1}$. As a result, from
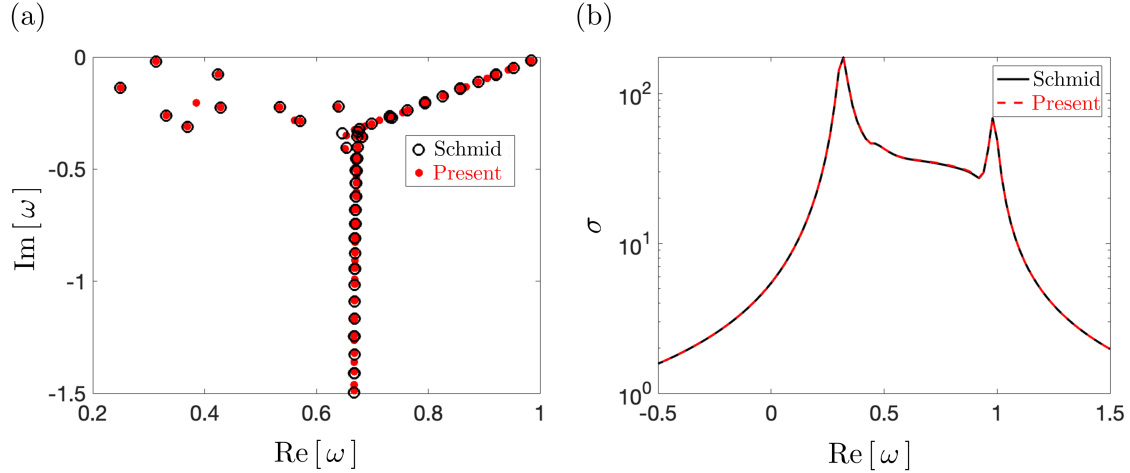
Fig. 1 **Validation results for a one-dimensional laminar channel flow at** $Re = 2000$**,** $\alpha = 1$**, and** $\beta = 0.1$**: (a) eigenspectrum and (b) resolvent gain. Colors: (black) Schmid and Brandt [25]; (red) present result.**

Eq. (17), the non-causal estimation kernel can be computed as

$$\hat{\boldsymbol{T}}_{z,nc} = \hat{\boldsymbol{G}}_r \hat{\boldsymbol{G}}_l^{-1} = \boldsymbol{S}_{z_1,y_1} \boldsymbol{S}_{y_1,y_1}^{-1}. \tag{22}$$

III. Validation

In this section, we present a series of test problems used to validate and demonstrate our implementation of the resolvent-based estimation tools within the CharLES framework.

A. Laminar channel flow

First, we used an incompressible laminar channel flow to validate the linear operator $\boldsymbol{A}$ constructed by our code. The base flow velocity is $[\bar{U}(y), 0, 0]$, where the streamwise component $\bar{U}(y) = 1 - y^2$ has a parabolic profile. The Reynolds number based on the channel half-height is $Re = 2000$, and the Mach number is set to $M = 0.1$ within our compressible code to mimic incompressibility. Since the base flow is invariant in the streamwise and spanwise directions, the disturbance field is Fourier-transformed into wavenumber space in these homogeneous directions. This yields a one-dimensional problem at each streamwise, spanwise wavenumber pair, providing a test of our source term formulation used to handle homogeneous directions. To assess the linear operator, we compute the eigenspectrum and resolvent gain for wavenumber pair $\alpha = 1$, $\beta = 0.1$. The results from our code are compared with those from the code provided by Schmid and Brandt [25] in Fig. 1. The close match provides a first indication that our linearizaton is working properly.
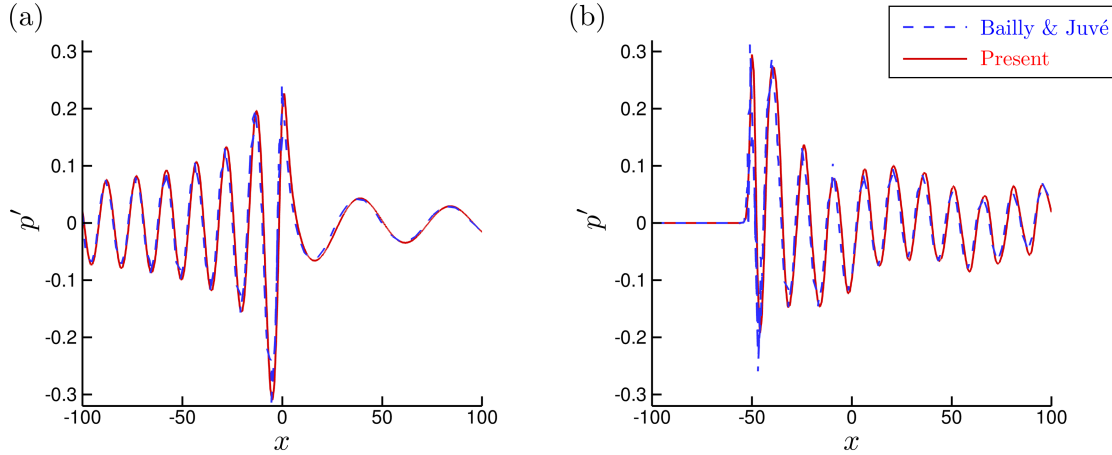
7

Fig. 2 **Pressure fluctuations as a result of acoustic radiation from a monopole: (a)** $M = 0.5$, $t = 270$, **source location** $(0, 1)$; **(b)** $M = 1.5$, $t = 304$, **source location** $(-50, 0)$. **Colors: (blue) Bailly and Juvé [26], (red) present result.**

B. Harmonic monopole source in a uniform meanflow

Second, we use the case of a harmonic monopole source in a uniform mean flow to validate the ability of our code to compute the response to a forcing term. Building estimation and control kernels require solutions to a series of linear runs (direct / adjoint) with an additional forcing, and this case allows us to test that aspect. We solve the two-dimensional Euler equations linearized about a uniform mean flow using the TVD-RK3 temporal scheme. The source term is

$$S(x, y, z, t) = \epsilon \exp\{-\alpha[(x - x_s)^2 + (y - y_s)^2]\} \sin(\omega t) \times [1, 0, 0, 1]^T,$$

where $\alpha = \ln(2)/2$ and x_s and y_s indicate the position of the monopole source term. This case was originally studied by Bailly and Juvé [26], and the reader is referred there for details. The results from our code are compared with those of Bailly and Juvé [26] for both a subsonic ($M = 0.5$) and a supersonic case ($M = 1.5$) in Fig. 2. We obtain a decent agreement for both cases.

C. Trailing line vortex

We validate the cylindrical extension to our solver using an inviscid trailing line vortex problem [27]. The baseflow is

$$\bar{u}_x(r) = e^{-r^2}, \qquad \bar{u}_r(r) = 0, \qquad \bar{u}_\theta(r) = \frac{q_s}{r}\left(1 - e^{-r^2}\right), \tag{23}$$

where q_s indicates the swirl intensity of the vortex. Accordingly, the modal ansatz is

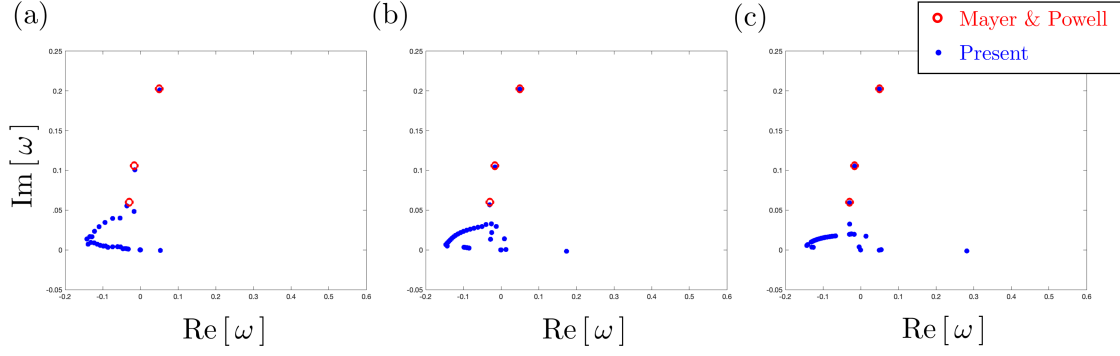$$q(x, r, \theta, t) = \bar{q}(r) + q'(x, r, \theta, t) \tag{24}$$

8

Fig. 3 **Stability of a one-dimensional inviscid trailing line vortex. Parameters:** $m = 1$, $q_s = -0.5$, $\alpha = 0.5$. **Grid convergence: (a)** $N_r = 201$, **(b)** $N_r = 401$, **(c)** $N_r = 801$. **Colors: (red) Mayer and Powell [27]; (blue) present result.**

with

$$q'(x, r, \theta, t) = \hat{q}(r)e^{i(\alpha x + m\theta - \omega t)}. \tag{25}$$

We set the streamwise and azimuthal wavenumbers to $\alpha = 0.5$ and $m = 1$, respectively, and compute the spectrum for three different grid sizes, $N_r = 201$, $N_r = 401$, and $N_r = 801$, where N_r is the number of points in the radial direction. The spectrum is compared with the three dominant unstable modes given by Mayer and Powell [27] in Fig. 3. Clearly, the eigenvalues computed using our code converge to the reference values as the grid is refined.

D. Turbulent airfoil wake

Recently, we applied the resolvent-based estimator to the turbulent flow over an airfoil [15]. Following Yeh and Taira [28], we consider a spanwise-periodic NACA0012 airfoil at chord-based Reynolds number $Re = 23,000$, Mach number $M = 0.3$, and angle of attack $AoA = 6°$. We first perform a large-eddy simulation (LES) of the flow using CharLES, and data from the simulation are used to construct the data-driven optimal non-causal and optimal causal estimation kernels, in addition to providing sensor data and target data to evaluate the accuracy of the estimates.

Fig. 4 shows sample estimation results for the turbulent airfoil [15]. We use the six shear-stress sensors shown in Fig. 4(a) to estimate the streamwise velocity at the indicated downstream target positions. Since the turbulent flow is three-dimensional, we consider multiple options for handling the spanwise coordinate. In Fig. 4(b-c), we exclusively estimate the spanwise-averaged fluctuations, while in Fig. 4(d-e) we estimate the fluctuations in the mid-span plane. The latter task is more challenging since the three-dimensional turbulent motions lead to fluctuations that are observed at the targets in the mid-span plane but cannot be sensed in that same plane. We are currently exploring whether additional out-of-plane sensors can improve the estimation accuracy. Nevertheless, it is clear in all cases that the causal resolvent-based estimator outperforms the truncated non-causal estimator and provides reasonable accuracy.
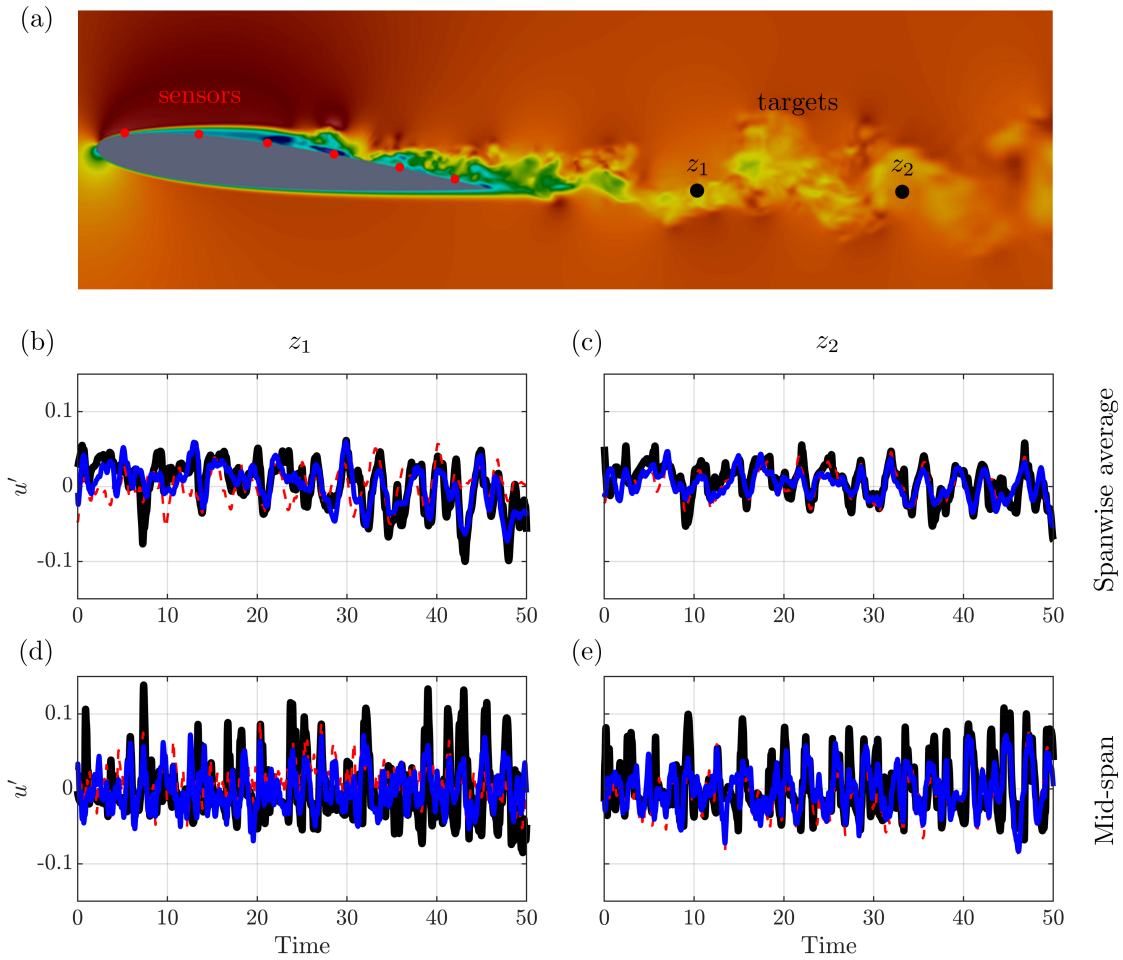
9

Fig. 4   Estimation results for a turbulent airfoil: (a) sensor and target placement; (b,c) target z_1; (c,e) target z_2; using (b,c) spanwise-averaged data; (d,e) mid-span data. Colors: (black) LES data; (pink) truncated non-causal method; (blue) optimal causal method.
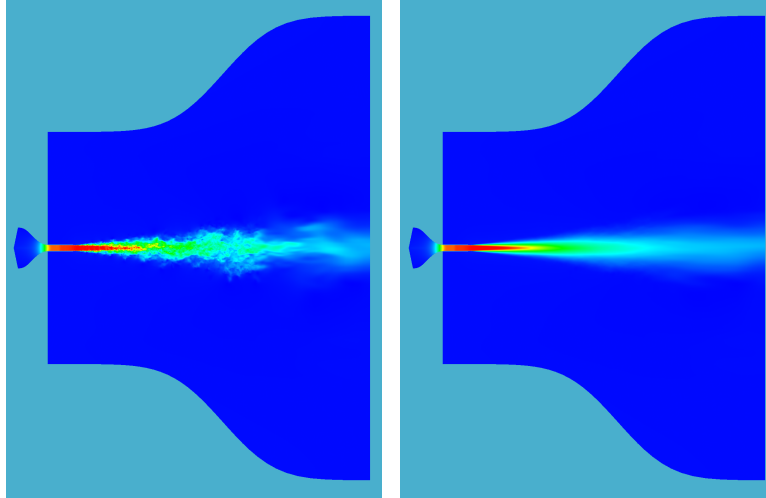
10

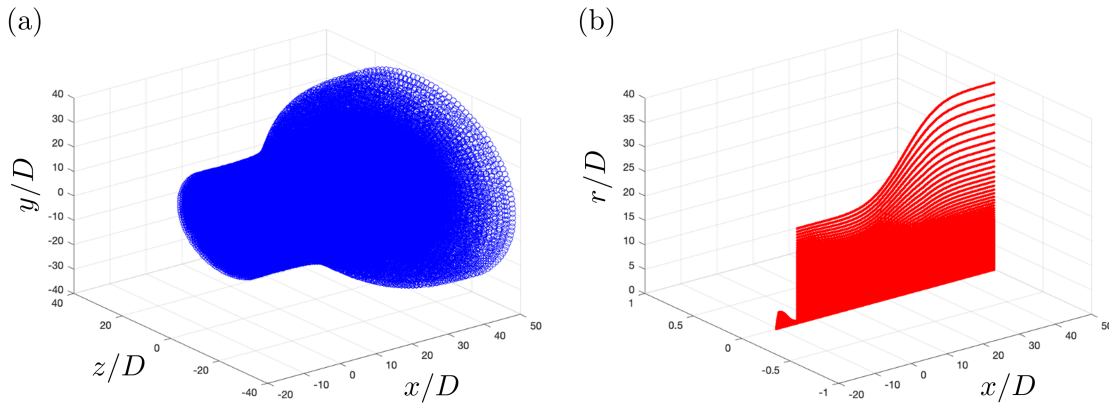**Fig. 5   The streamwise velocity for the Mach 0.9 subsonic jet: (left) instantaneous snapshot; (right) time-averaged mean.**

(a)   (b)

Fig. 6   Grids for the subsonic jet: (a) three-dimensional unstructured LES grid (b) two-dimensional structured (axisymmetric) grid used for the linear simulations.

IV. Jet results

In this section, we describe our initial application of the resolvent-based tools implemented within CharLES to a jet.

A. Problem setup and mean flow

While our ultimate interest is supersonic jets, we present some preliminary results for a subsonic jet configuration. The Mach number is $M_j = 0.9$, the Reynolds number based on the jet-exit conditions and the jet diameter is $Re = 10^6$, and the jet is isothermal ($T_j/T_\infty = 1$). This same setup was simulated via LES by Brès et al. [29], and we use data from that simulation made available in the public database assembled by Towne et al. [30]. The full domain of the jet is shown in Fig. 5.

To perform the linear operator-based calculations, the axisymmetric mean flow from the three-dimensional

11

unstructured LES grid containing ≈ 15.9 million control volumes, shown in Fig. 6(a), is interpolated onto a two-dimensional structured grid in the $x - r$ plane containing 196994 control volumes, shown in Fig. 6(b). The structured grid in the plume region is similar to the grid used in the resolvent calculations of Schmidt et al. [4], except that we have added more points along the nozzle-lip in the radial direction.

B. Resolvent Analysis

To further test our linear operators for the actual jet case, we begin by performing a resolvent analysis for the subsonic jet (using the LES mean flow interpolated unto the two-dimensional grid described in the previous section) for four different azimuthal wavenumbers m = 0, 1, 2, and 3. Analogous to the discussion in Sec II.C, the resolvent operator is augmented with operators $\boldsymbol{B}_f$ and $\boldsymbol{C}_z$ to restrict the inputs and outputs to the plume region, i.e., $\boldsymbol{R}_{zf}(\omega) = \boldsymbol{C}_z(-i\omega\boldsymbol{I} - \boldsymbol{A})^{-1}\boldsymbol{B}_f$. Overall, this setup matches that of Schmidt et al. [4] with one critical difference: the present calculation includes the nozzle. As a result, we don't expect the gains to exactly match those from Schmidt et al. [4]; we are only looking for qualitative agreement.

The resolvent gains computed for a range of Strouhal numbers are shown in Fig. 7. The trend largely follows that of Schmidt et al. [4] with one main difference. At the higher frequencies, we see additional growth/peaks in the current results. We believe these to be related to the resonance of trapped acoustic modes in the jet core, and the bands of Strouhal number for which these peaks are observed agree with the values given in Towne et al. [31] for azimuthal wavenumbers m = 0 and m = 1. The stronger presence of these waves in the present results is a consequence of including the nozzle in the geometry, allowing for stronger resonance compared to the previous calculations containing a sponge region at the jet inlet plane. The optimal input and output modes for m = 0 and St = 0.4 are shown in Fig. 8. The input and output modes contain the expected near-nozzle forcing and wavepacket response, respectively, but also contain prominent trapped acoustic waves in the potential core not visible in Schmidt et al. [4], consistent with the discussion of the gains above.

C. Operator-based & data-driven estimation

Next, we apply the operator-based and data-driven resolvent-based estimation methods to estimate wavepackets within the jet. For brevity, we restrict our attention to axisymmetric disturbances (m = 0).

First, we use single and multi-stage linear (direct and/or adjoint) runs to efficiently build the operator-based estimation kernels using the procedures described in Martini et al. [13] and summarized in Sec. II. The result of one such linear run (direct run of the actuator system) is shown in Fig. 9. The actuator is placed close to the nozzle-lip. The linear response is recorded, and a snapshot showing pressure disturbances t = 15 acoustic time units after perturbing the actuator is shown in Fig. 9. To perform estimation, a linear adjoint-direct run of the sensor system needs to be performed as given in Martini et al. [13]. A sensor is first perturbed in an adjoint run. Later, the results from this run are used to force
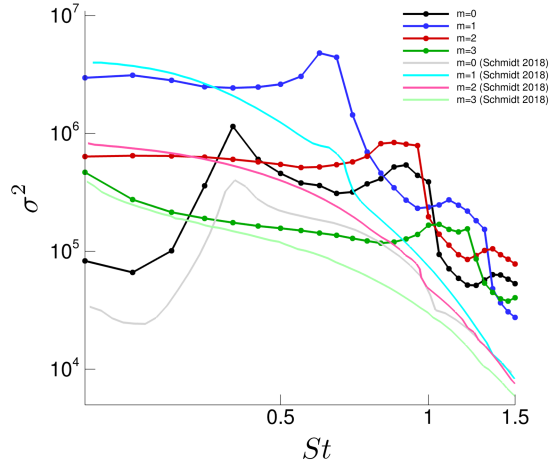
Fig. 7 Resolvent gain as a function of Strouhal number for a Mach 0.9 subsonic round jet for azimuthal wavenumbers $m = 0, 1, 2, 3$. Results compared with Schmidt et al. [4].
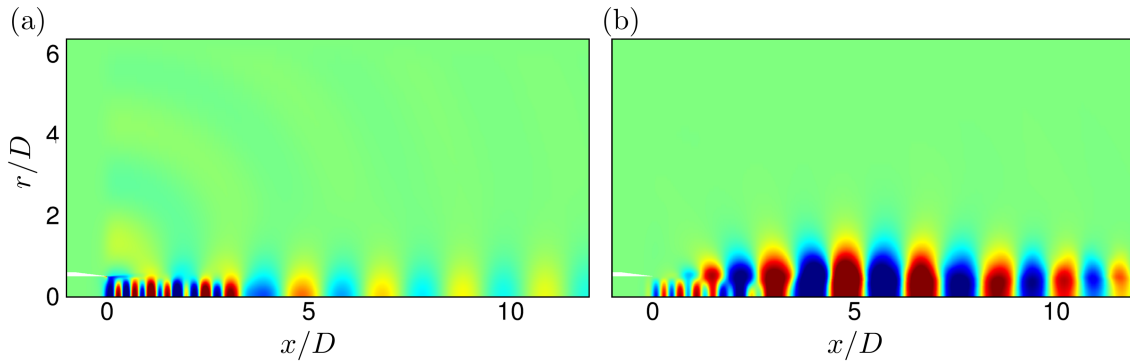

Fig. 8 Pressure component of the optimal (a) input and (b) output modes for a Mach 0.9 subsonic round jet for $m = 0$ and $St = 0.4$.

a direct run, and the sensor and target data are recorded. The estimation kernel is then formed as given in Eq. (17). Second, we use the data-driven tools described in Sec. II.D to construct the estimation kernel using Eq. (22).

For both the operator-based and data-driven cases, we use measurements y and targets z consisting of the streamwise velocity perturbations at single points in the jet. We consider two configurations, shown in Fig. 10. In the first configuration, the sensor is placed at $(x/D, r/D) = (0.3, 0.55)$, and in the second configuration, it is placed at $(2.0, 0.0)$. In both cases, the target is located at $(3, 0)$. We use both the optimal non-causal kernel in Eq. (17) and the truncated non-causal kernel in which the non-causal kernel is set to zero for future times. The estimation is then carried out via the convolution in Eq. (14). Both the sensor reading $y(t)$ and the ground-truth target $z(t)$ against which the estimation results are compared are taken from the LES data [29, 30].

The estimation results for both configurations using both the operator and data-driven methods, along with the corresponding estimation kernels, are shown in Fig. 11. The operator-based and data-driven kernels are quite similar,
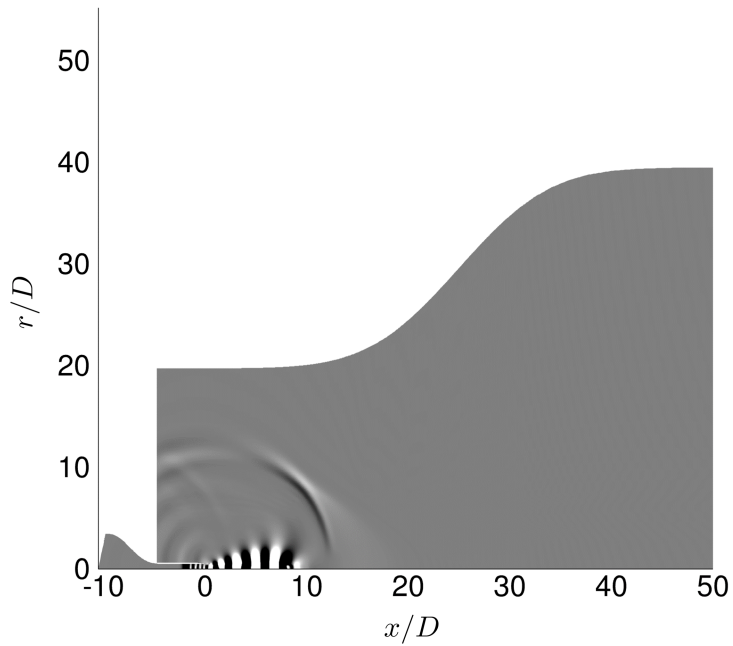
13

Fig. 9   A linear impulse response to perturbing an actuator placed near the nozzle-lip (0.1,0.6) at $t = 15$ **acoustic units (direct run).**
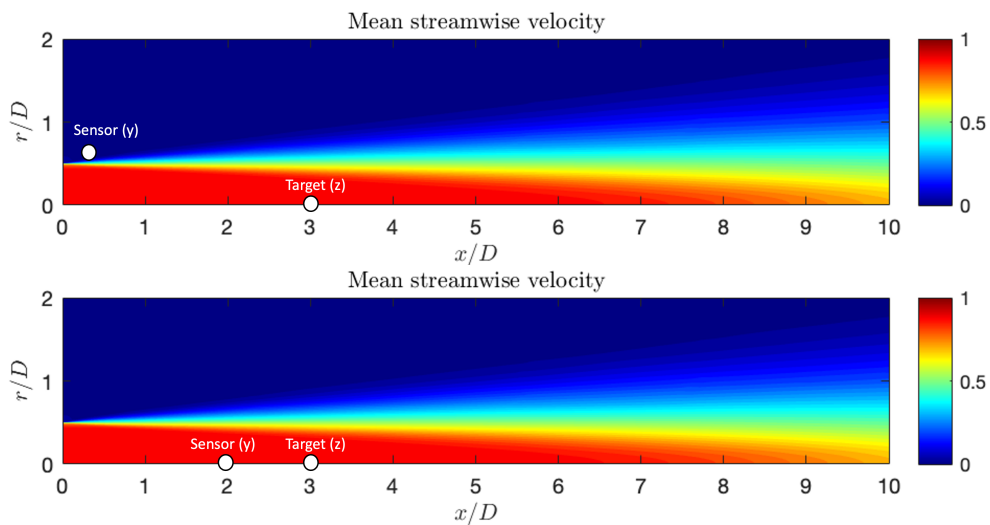

Fig. 10   Sensor placement and target selection for two configurations: (top) configuration 1; (bottom) configuration 2. The contours show the mean streamwise velocity in the plume region for reference.
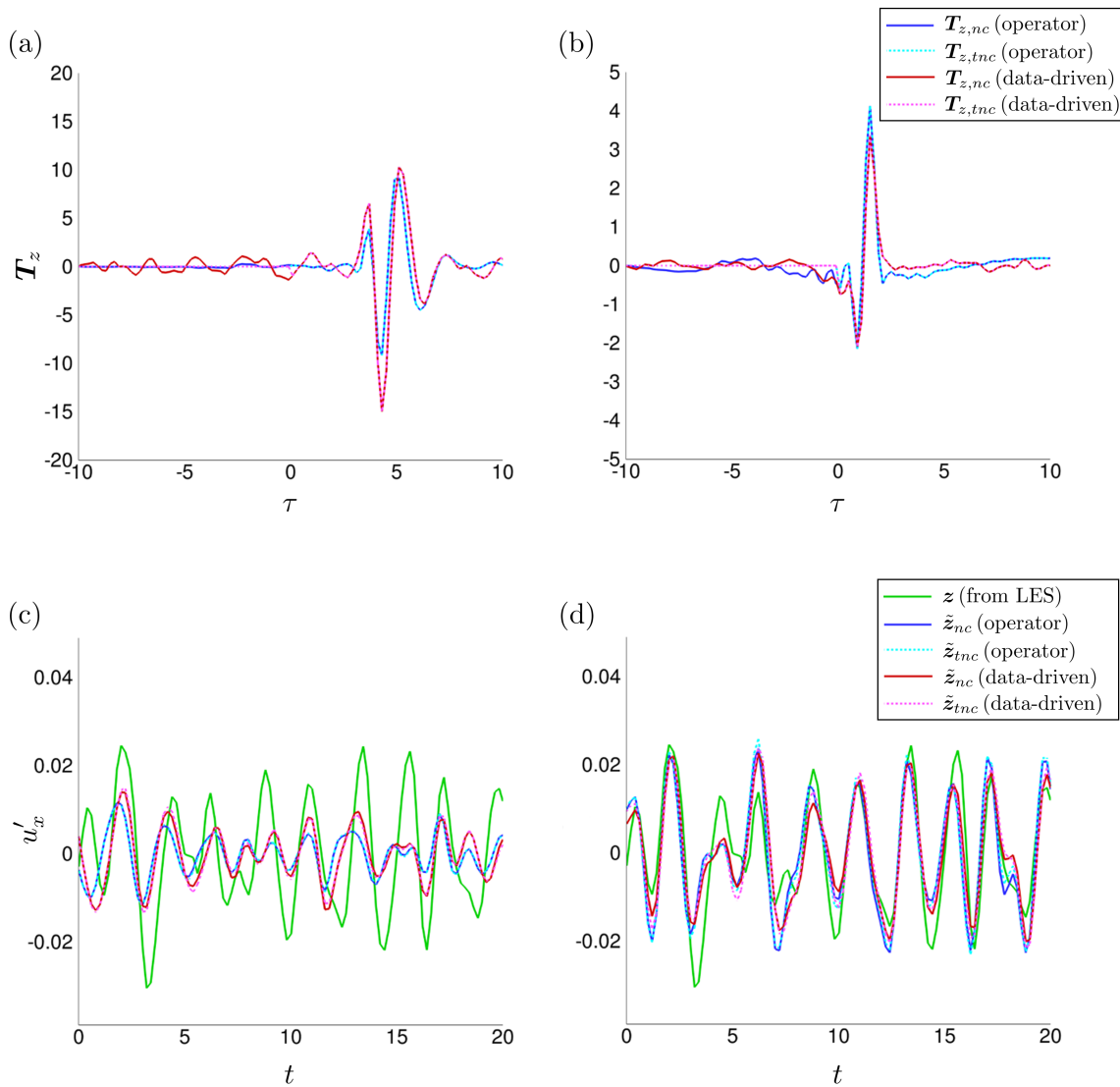
Fig. 11 Estimation of the axisymmetric component of the streamwise velocity for the subsonic jet. Rows: (a,b) estimation kernels; (c,d) estimation target results. Columns: (a,c) configuration 1; (b,d) configuration 2.
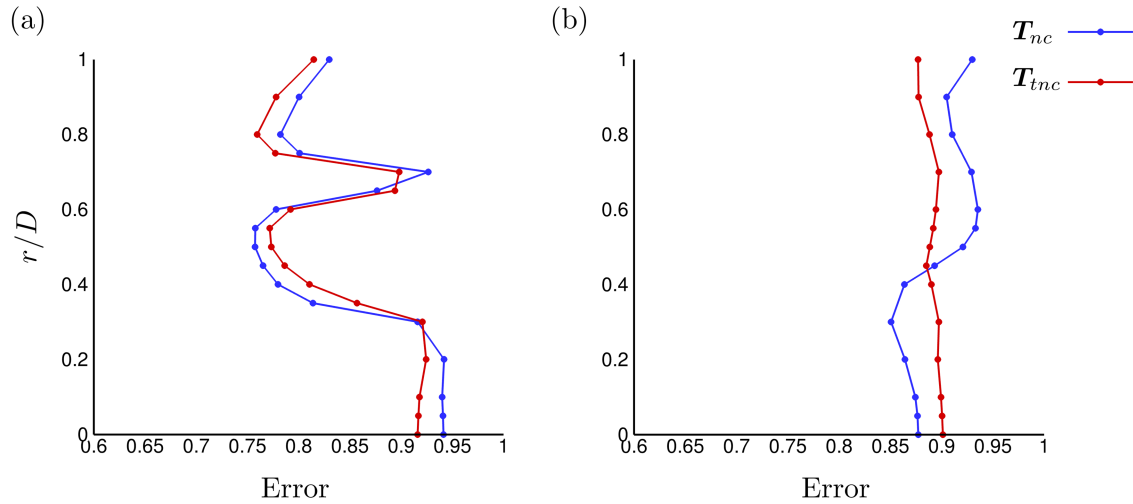
Fig. 12   Impact on estimation error of the radial position of a near-nozzle sensor measuring (a) streamwise velocity and (b) pressure. Colors: (blue) optimal non-causal estimator; (red) truncated non-causal estimator.

exhibiting the same peaks and dominant frequency. The τ values of the peaks are associated with the time required for the strongest wavepackets to travel from the sensor location to the target location. It is apparent that the operator-based kernels are naturally causal (even though we did not explicitly force them to be), as their value is zero for $\tau < 0$. The data-driven kernels have a small non-causal component, which is likely due to incomplete statistical convergence. Due to the similarity of the operator-based and data-driven kernels, the estimation results delivered by the two methods are similar for both configurations. The performance for configuration 2 is much better; it is intuitive that the estimation would be difficult in the first case and easier in the second given the closer proximity of the sensor to the target in the latter case. Nevertheless, the estimators successfully predict the dominant frequencies for both configurations.

Optimizing the sensor quantity, types, and locations is a central part of our ongoing work. As a first study, we next investigate the impact of the radial position and measured quantity of the near-nozzle sensor in configuration 1. Fig. 12 shows the estimation error as a function of the radial position using (a) streamwise velocity measurements as in the previous cases and (b) pressure measurements. When using streamwise velocity measurements, the lowest error is obtained when the sensor is placed just outside of the jet shear layer at $(r/D) = 0.55$. This is encouraging from a practical perspective, as placing sensors outside of the jet is more realistic than inside the jet, especially for hot jets typical of real applications. The shape of the error curve can be explained by the radial structure of the Kelvin-Helmholtz eigenmodes that generate wavepackets. Specifically, low error is observed where the amplitude of the Kelvin-Helmholtz eigenfunction is high and vice versa. When pressure is measured, the optimal radial location is inside of the jet, and the error level is higher, indicating that velocity measurements are likely preferable. While the error levels are higher than one would like in all cases, they can be reduced by adding additional sensors. These results will be reported in a future publication.

D. Coherence

A useful metric that can give a sense of how well a certain sensor is expected to estimate the signal at a given target is the coherence between the sensor and the target signals. This sensor-target coherence is given in terms of CSDs as

$$\hat{\boldsymbol{\gamma}}_{zy}(\omega) = \frac{|\hat{\boldsymbol{S}}_{zy}(\omega)|}{\sqrt{\hat{\boldsymbol{S}}_{yy}(\omega)}\sqrt{\hat{\boldsymbol{S}}_{zz}(\omega)}} \ . \tag{26}$$

Probing the sensor-target coherence can provide guidance on questions like: (i) Which of two candidate sensor-target configurations is likely to produce better estimation results? (ii) Can we get a performance benefit by moving the target further upstream or away from the axis? (iii) Which physical quantities should be chosen to measure the signal at the sensor and the target?

As an example, the coherences for four different combinations of sensor-target positions are shown in Fig. 13. Here, Fig. 13(a) and Fig. 13(d) are the same as the aforementioned configuration 1 and configuration 2, respectively. It can clearly be seen that the coherence values for configuration 2 are much higher, as expected. It can be seen in Fig. 13(b) that there might be a significant performance benefit to moving the target slightly upstream to $(x/D, r/D) = (2, 0)$ when using a near-nozzle sensor. However, whether there is a cost to doing this, in terms of the efficacy of achieving far-field noise reduction by canceling noise-generating wavepackets, remains to be seen. There are several such choices to be made in designing an effective estimation (and control) strategy, and coherence can serve as a guiding metric [3, 16].

V. Conclusions and future work

This paper has presented some initial steps toward our long-term objective of realizing a realistic resolvent-based strategy for reducing the far-field noise produced by wavepackets in high-speed, turbulent jets. This includes the implementation and validation of the resolvent-based tools within the CharLES simulation framework and preliminary estimation results for a Mach 0.9 jet. Analogous analyses have already been completed for an incompressible flow over a backward-facing step [13] and laminar and turbulent flow over a NACA 0012 airfoil [14, 15]; here, we are extending these and applying similar techniques to high-speed turbulent jets.

Future work will include applying the resolvent-based estimation and control tools with causality enforced by a Wiener-Hopf formalism to the case of the Mach 0.9 isothermal jet with the aim of reducing far-field noise. The effect of sensor, actuator, and target placement and the effectiveness of different combinations thereof will be studied. We will also extend this study to two additional cases, Mach 1.5 ideally expanded and overexpanded supersonic jets [17]. We have completed large-eddy simulations of these cases (see Fig .14) and are working toward repeating the analyses presented in this paper.
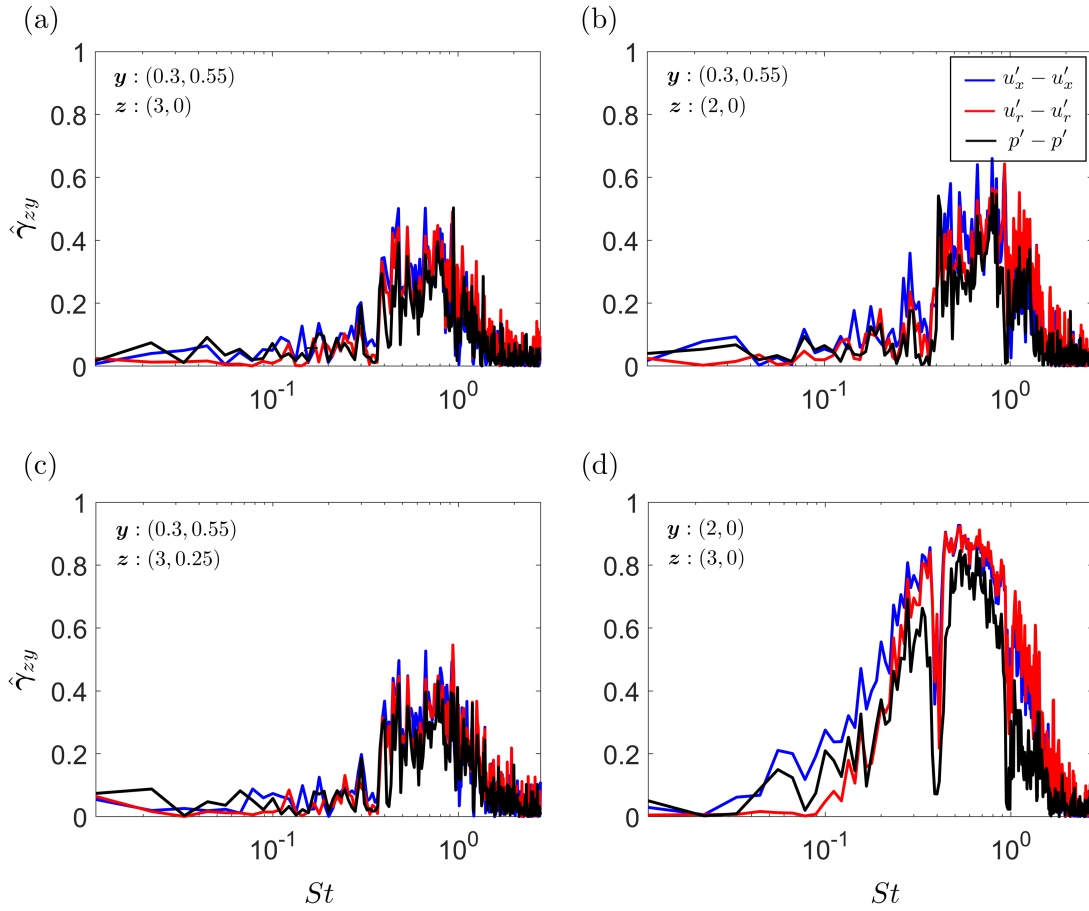
Fig. 13   Coherence between the axisymmetric ($m = 0$) component of the signal at the sensor y and the target z; colors indicate the physical quantity used for the sensor and target measurement: (blue) $u'_x - u'_x$; (red) $u'_r - u'_r$; (black) $p' - p'$.
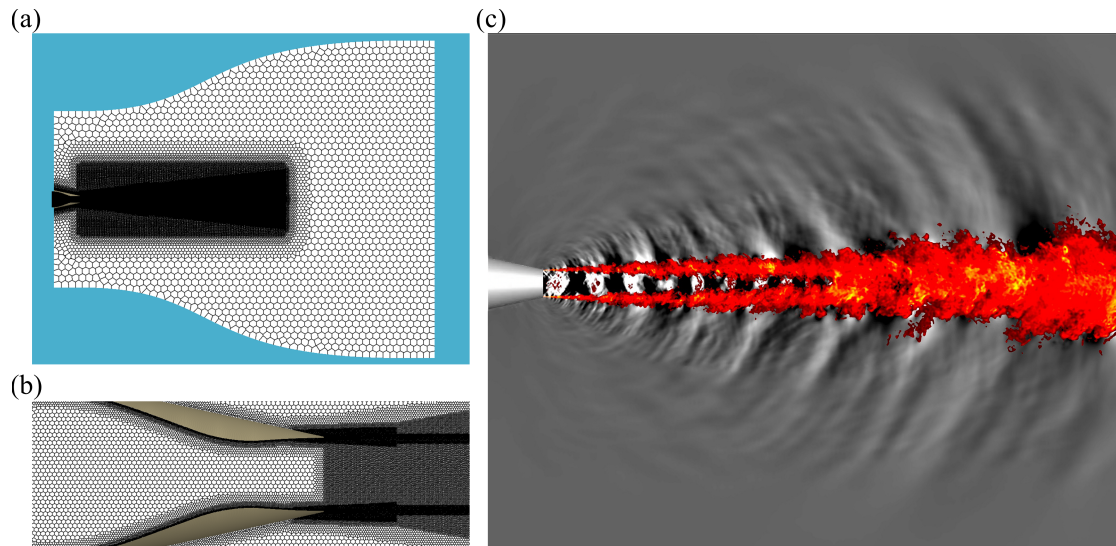
Fig. 14 Large-eddy simulations performed for a Mach 1.5 supersonic Jet: (a) the full simulation domain and grid; (b) close-up view of the grid in the near-nozzle region; (c) instantaneous snapshot showing temperature (color) and pressure (grayscale).

Acknowledgements

References

[1] Henderson, B., "Fifty Years of Fluidic Injection for Jet Noise Reduction," *International Journal of Aeroacoustics*, Vol. 9, No. 1-2, 2010, pp. 91–122. https://doi.org/10.1260/1475-472X.9.1-2.91.

[2] Sinha, A., Towne, A., Colonius, T., Schlinker, R. H., Reba, R., Simonich, J. C., and Shannon, D. W., "Active Control of Noise from Hot Supersonic Jets," *AIAA Journal*, Vol. 56, No. 3, 2018, pp. 933–948. https://doi.org/10.2514/1.J056159.

[3] Maia, I. A., Jordan, P., Cavalieri, A. V. G., Martini, E., Sasaki, K., and Silvestre, F. J., "Real-time reactive control of stochastic disturbances in forced turbulent jets," *Physical Review Fluids*, Vol. 6, 2021, p. 123901. https://doi.org/10.1103/PhysRevFluids.6.123901.

[4] Schmidt, O. T., Towne, A., Rigas, G., Colonius, T., and Brès, G. A., "Spectral analysis of jet turbulence," *Journal of Fluid Mechanics*, Vol. 855, 2018, p. 953–982. https://doi.org/10.1017/jfm.2018.675.

[5] Pickering, E., Towne, A., Jordan, P., and Colonius, T., "Resolvent-based modeling of turbulent jet noise," *The Journal of the Acoustical Society of America*, Vol. 150, No. 4, 2021, pp. 2421–2433. https://doi.org/10.1121/10.0006453.

[6] Karban, U., Bugeat, B., Towne, A., Lesshafft, L., Agarwal, A., and Jordan, P., "An empirical model of noise sources in subsonic jets," *Journal of Fluid Mechanics*, Vol. 965, 2023, p. A18. https://doi.org/10.1017/jfm.2023.376.

[7] Towne, A., Schmidt, O. T., and Colonius, T., "Spectral proper orthogonal decomposition and its relationship to dynamic mode decomposition and resolvent analysis," *Journal of Fluid Mechanics*, Vol. 847, 2018, p. 821–867. https://doi.org/10.1017/jfm.2018.283.

[8] McKeon, B. J., and Sharma, A. S., "A critical-layer framework for turbulent pipe flow," *Journal of Fluid Mechanics*, Vol. 658, 2010, p. 336–382. https://doi.org/10.1017/S002211201000176X.

[9] Beneddine, S., Sipp, D., Arnault, A., Dandois, J., and Lesshafft, L., "Conditions for validity of mean flow stability analysis," *Journal of Fluid Mechanics*, Vol. 798, 2016, pp. 485–504. https://doi.org/10.1017/jfm.2016.331.

[10] Towne, A., Lozano-Durán, A., and Yang, X., "Resolvent-based estimation of space–time flow statistics," *Journal of Fluid Mechanics*, Vol. 883, 2020, p. A17. https://doi.org/10.1017/jfm.2019.854.

[11] Martini, E., Cavalieri, A. V. G., Jordan, P., Towne, A., and Lesshafft, L., "Resolvent-based optimal estimation of transitional and turbulent flows," *Journal of Fluid Mechanics*, Vol. 900, 2020, p. A2. https://doi.org/10.1017/jfm.2020.435.

[12] Amaral, F. R., Cavalieri, A. V., Martini, E., Jordan, P., and Towne, A., "Resolvent-based estimation of turbulent channel flow using wall measurements," *Journal of Fluid Mechanics*, Vol. 927, 2021, p. A17. https://doi.org/10.1017/jfm.2021.764.

[13] Martini, E., Jung, J., Cavalieri, A. V., Jordan, P., and Towne, A., "Resolvent-based tools for optimal estimation and control via the Wiener–Hopf formalism," *Journal of Fluid Mechanics*, Vol. 937, 2022, p. A19. https://doi.org/10.1017/jfm.2022.102.

[14] Jung, J., Bhagwat, R., and Towne, A., "Resolvent-based estimation of laminar flow around an airfoil," *AIAA Paper #2023-0077*, 2023. https://doi.org/10.2514/6.2023-0077.

[15] Jung, J., and Towne, A., "Toward turbulent wake estimation using a resolvent-based approach," *AIAA Paper #2024-0057*, 2024. https://doi.org/10.2514/6.2024-0057.

[16] Audiffred, D., Cavalieri, A., Maia, I., Martini, E., and Jordan, P., "Reactive experimental control of turbulent jets," *arXiv:2402.10860*, 2024. https://doi.org/10.48550/arXiv.2402.10860.

[17] Brès, G. A., Ham, F. E., Nichols, J. W., and Lele, S. K., "Unstructured Large-Eddy Simulations of Supersonic Jets," *AIAA Journal*, Vol. 55, No. 4, 2017, pp. 1164–1184. https://doi.org/10.2514/1.J055084.

[18] Nielsen, E. J., and Kleb, W. L., "Efficient Construction of Discrete Adjoint Operators on Unstructured Grids Using Complex Variables," *AIAA Journal*, Vol. 44, No. 4, 2006, pp. 827–836. https://doi.org/10.2514/1.15830.

[19] Cook, D., Thome, J., Brock, J., Nichols, J., and Candler, G., "Understanding effects of nose-cone bluntness on hypersonic boundary layer transition using input-output analysis," *AIAA Paper #2018-0378*, 2018. https://doi.org/10.2514/6.2018-0378.

[20] Balay, S., Abhyankar, S., Adams, M. F., Benson, S., Brown, J., Brune, P., Buschelman, K., Constantinescu, E. M., Dalcin, L., Dener, A., Eijkhout, V., Faibussowitsch, J., Gropp, W. D., Hapla, V., Isaac, T., Jolivet, P., Karpeev, D., Kaushik, D., Knepley, M. G., Kong, F., Kruger, S., May, D. A., McInnes, L. C., Mills, R. T., Mitchell, L., Munson, T., Roman, J. E., Rupp, K., Sanan, P., Sarich, J., Smith, B. F., Zampini, S., Zhang, H., Zhang, H., and Zhang, J., "PETSc Web page," , 2022. URL https://petsc.org/.

[21] Balay, S., Abhyankar, S., Adams, M. F., Benson, S., Brown, J., Brune, P., Buschelman, K., Constantinescu, E., Dalcin, L., Dener, A., Eijkhout, V., Faibussowitsch, J., Gropp, W. D., Hapla, V., Isaac, T., Jolivet, P., Karpeev, D., Kaushik, D., Knepley, M. G., Kong, F., Kruger, S., May, D. A., McInnes, L. C., Mills, R. T., Mitchell, L., Munson, T., Roman, J. E., Rupp, K., Sanan, P., Sarich, J., Smith, B. F., Zampini, S., Zhang, H., Zhang, H., and Zhang, J., "PETSc/TAO Users Manual," Tech. Rep. ANL-21/39 - Revision 3.18, Argonne National Laboratory, 2022.

[22] Bhagwat, R., "Development of stability analysis tools for high speed compressible flows," Ph.D. thesis, North Carolina State University, 2020. URL https://www.lib.ncsu.edu/resolver/1840.20/38676.

[23] Martini, E., Rodríguez, D., Towne, A., and Cavalieri, A. V., "Efficient computation of global resolvent modes," *Journal of Fluid Mechanics*, Vol. 919, 2021, p. A3. https://doi.org/10.1017/jfm.2021.364.

[24] Farghadan, A., Martini, E., and Towne, A., "Scalable resolvent analysis for three-dimensional flows," *arXiv:2309.04617*, 2023. https://doi.org/10.48550/arXiv.2309.04617.

[25] Schmid, P. J., and Brandt, L., "Analysis of Fluid Systems: Stability, Receptivity, Sensitivity: Lecture notes from the FLOW-NORDITA Summer School on Advanced Instability Methods for Complex Flows, Stockholm, Sweden, 2013," *Applied Mechanics Reviews*, Vol. 66, No. 2, 2014. https://doi.org/10.1115/1.4026375.

[26] Bailly, C., and Juvé, D., "Numerical Solution of Acoustic Propagation Problems Using Linearized Euler Equations," *AIAA Journal*, Vol. 38, No. 1, 2000, pp. 22–29. https://doi.org/10.2514/2.949.

[27] Mayer, E. W., and Powell, K. G., "Viscous and inviscid instabilities of a trailing vortex," *Journal of Fluid Mechanics*, Vol. 245, 1992, p. 91–114. https://doi.org/10.1017/S0022112092000363.

[28] Yeh, C.-A., and Taira, K., "Resolvent-analysis-based design of airfoil separation control," *Journal of Fluid Mechanics*, Vol. 867, 2019, pp. 572–610. https://doi.org/10.1017/jfm.2019.163.

[29] Brès, G. A., Jordan, P., Jaunet, V., Le Rallic, M., Cavalieri, A. V. G., Towne, A., Lele, S. K., Colonius, T., and Schmidt, O. T., "Importance of the nozzle-exit boundary-layer state in subsonic turbulent jets," *Journal of Fluid Mechanics*, Vol. 851, 2018, p. 83–124. https://doi.org/10.1017/jfm.2018.476.

[30] Towne, A., Dawson, S. T. M., Brès, G. A., Lozano-Durán, A., Saxton-Fox, T., Parthasarathy, A., Jones, A. R., Biler, H., Yeh, C.-A., Patel, H. D., and Taira, K., "A Database for Reduced-Complexity Modeling of Fluid Flows," *AIAA Journal*, Vol. 61, No. 7, 2023, pp. 2867–2892. https://doi.org/10.2514/1.J062203.

[31] Towne, A., Cavalieri, A. V. G., Jordan, P., Colonius, T., Schmidt, O., Jaunet, V., and Brès, G. A., "Acoustic resonance in the potential core of subsonic jets," *Journal of Fluid Mechanics*, Vol. 825, 2017, p. 1113–1152. https://doi.org/10.1017/jfm.2017.346.